SUPPLEMENT TO THE *WELDING JOURNAL*, JANUARY 2018
Sponsored by the American Welding Society

Toward Process-Based Quality through a Fundamental Understanding of Weld Microstructural Evolution

Qualifying welded components by integrating software and hardware tools that are capable of describing physical processes that occur during welding was explored

BY SUDARSANAM SURESH BABU

ABSTRACT

In this overview paper, the possibility of qualifying welded components by integrating software and hardware tools that are capable of describing physical processes that occur during welding is explored. The existing and emerging tools to define geometrical boundary conditions, process parameters, heat and mass transfer, solidification, solid-state transformation, plastic deformation, distortion, residual stress, and performance of welded components are reviewed. Existing challenges relevant to the fundamental understanding of complex alloying, processing environment, and transients in energy deposition are discussed with reference to microstructure evolution. Approaches to address these challenges were articulated with published case studies relevant to welding and additive manufacturing.

KEYWORDS

• Process-Based Quality • Microstructural Evolution • Energy Deposition
• Additive Manufacturing • Residual Stress

Introduction and Motivation

In 2000, the American Welding Society developed a road map (Ref. 1) with the following goals: 1) Increase the uses of welding by 25%, decrease the cost, and increase the productivity; 2) enhance the process technology that allows for the use of welding across all manufacturing sectors; 3) develop new welding technology along with new materials so that it can be used for all applications; 4) ensure that welding can be part of the six-sigma quality environment; 5) increase the knowledge base of people employed at all levels of the welding industry; and 6) reduce energy use by 50% through productivity improvements. To meet these goals, a research and development pathway (Ref. 2), spanning from 2000 to 2040, that integrates the process and computational modeling, including process-based quality was articulated — Fig. 1. Interestingly, rapid qualification of goods and components is critical to existing applications that are based on traditional supply chain with slow and serial flow of information, materials and performance expectations, as well as emerging trends such as smart manufacturing that will rely on an agile and integrative approach facilitated by close coupling of technologies (Refs. 3, 4) relevant to the whole manufacturing life cycle. The manufacturing life cycle (Ref. 5) involves design, selection of materials, selection of process and environment, deployment of robotics and automation, certification through destructive testing of simulative samples and nondestructive evaluation (NDE), followed by recycling and rejuvenation at the end of useful life. Since fusion welding, solid-state joining, brazing, and soldering are crucial to the above manufacturing life cycle (Ref. 6), this paper explores the feasibility of ensuring the quality of welded components through modification of process parameters based on a fundamental understanding of microstructural evolution. Note that this paper is not a comprehensive review, and readers are referred to various publications throughout the document for an in-depth review.

Current Methodologies and Process-Based Quality

The AWS *Welding Handbook* classifies the technologies relevant to the joining of advanced materials into eight categories including arc welding, solid-state joining, resistance welding, oxyfuel gas welding, brazing, soldering, and other allied processes. A quick accounting of these categories and subclassifications shows there are more than 70 processes (Ref. 7). At the same time, there are hundreds of structural metals and alloys based on iron, aluminum, copper, magnesium,

https://doi.org/10.29391/2018.97.001

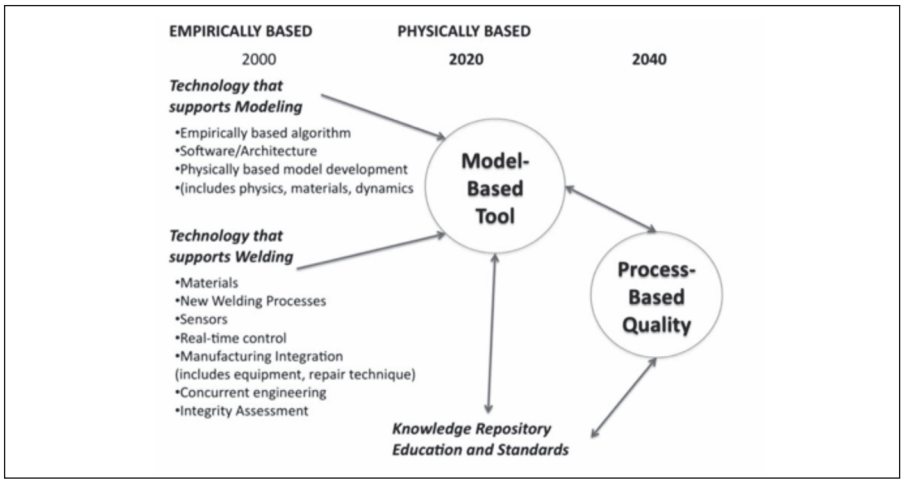

Fig. 1 — Schematic of research and development roadmap spanning four decades developed by AWS in the year 2000.

titanium, zinc, tin, lead, nickel, cobalt, zirconium, hafnium, and precious and refractory metals (Ref. 8).

As a result of the large number of permutations that is possible based on the above options, the industry has taken a cautious and pragmatic approach of deploying joining processes through simulative tests, qualification, and certification defined by the standards (Ref. 9). These are usually documented in terms of Welding Procedure Specifications (WPSs) (Ref. 10) and Procedure Qualification Records (PQRs) (Ref. 11), and often used as transactional documents between the end user of welds and the provider of fabrication services. These foundational standards published by AWS (Refs. 12, 13) and other organizations have gained the confidence and trust of industry allowing for welding to be used as a common tool for critical applications. For example, the American Petroleum Institute (API) has published standards for welding of pipelines (API 1104) that specify various aspects including equipment, materials, manual and automatic procedures, welding with and without welding wires, welders, design and preparation of joint geometry, inspection and testing of welds, repair and removal of defects, procedures for nondestructive testing, and acceptance tests based on NDE (Ref. 14). With emerging critical applications, these standards may become prescriptive and will not allow flexibility to minimize the variability of expected performance in service. As a result, the engineering advance will be a single point solution specific to a given geometry and application.

In addition, because WPSs and PQRs are developed with an extensive amount of resources, they are not openly disseminated to the public in peer-reviewed papers. As a result, many innovative and engineering solutions may remain proprietary and part of transactional documents. With every new application, every entity has to repeat the above procedures, again and again, thereby limiting the agility of the welding and joining industry to adopt new processes and materials while maintaining the trust of customers. This leads to the fundamental question: is there a possibility of qualifying welded components with varying geometries by characterizing the processes within the context of existing standards with minimal trial and error experimentation?

Process-based quality is defined as material and information flow where all aspects of welding life cycle, i.e., design, materials, process, and estimation of performance are considered and evaluated simultaneously. A typical process-based quality flow will involve concurrent activities ranging from modeling to making and measuring. In the modeling step, the geometry of the component (e.g., fillet weld geometry) for a given application is designed with knowledge from material properties (e.g., yield strength and residual stress) predicted by integrated process models for a given process (e.g., laser welding) based on boundary conditions (Ref. 15). In the making step, the boundary conditions (e.g., welding current, weaving, speed, restraints, etc.) are recorded and provided as input to the modeling activity. In the measuring step, responses of the material to process (e.g., temperature distribution, geometric displacements, and cracking) are measured using in-situ sensors. With the information from all these activities, a welding engineer may be able to qualify a component for final service with minimal destructive testing and NDE.

Existing Tools for Process-Based Quality

Many aspects of the process-based quality approach have already been addressed by welding researchers through development of empirical, phenomenological, physics-based modeling tools for computational weld mechanics (Refs. 16, 17), as well as, deployment of in-situ sensors (Ref. 18), controls (Ref. 19), and data logging devices (Ref. 20). These tools focus on comprehensive descriptions of boundary conditions for welding (Ref. 21), heat and mass transfer (Refs. 22, 23), solidification (Ref. 24), solid-state phase transformation (Refs. 25, 26), transient thermal stresses (Ref. 27), elastic and plastic deformation (Ref. 28), incipient crack formation (Ref. 29), residual stress, and distortion evolution (Ref. 30). These aspects are briefly reviewed below.

Description of Geometry, Material, and Processing Boundary Conditions

It is well known from engineering fundamentals that boundary conditions have a great influence on the outcome of any model predictions. For example, in welding and joining, these boundary conditions include the initial geometry of the joints, restraints used for holding the joints, thermal conductivity of the substrate, locked-in residual stress within the incoming materials, variations in compositions of the base material and filler materials, and transients in the heat source movement.

Pahkamaa et al. (Ref. 31) have demonstrated the complex interrelationship between variations in geome-

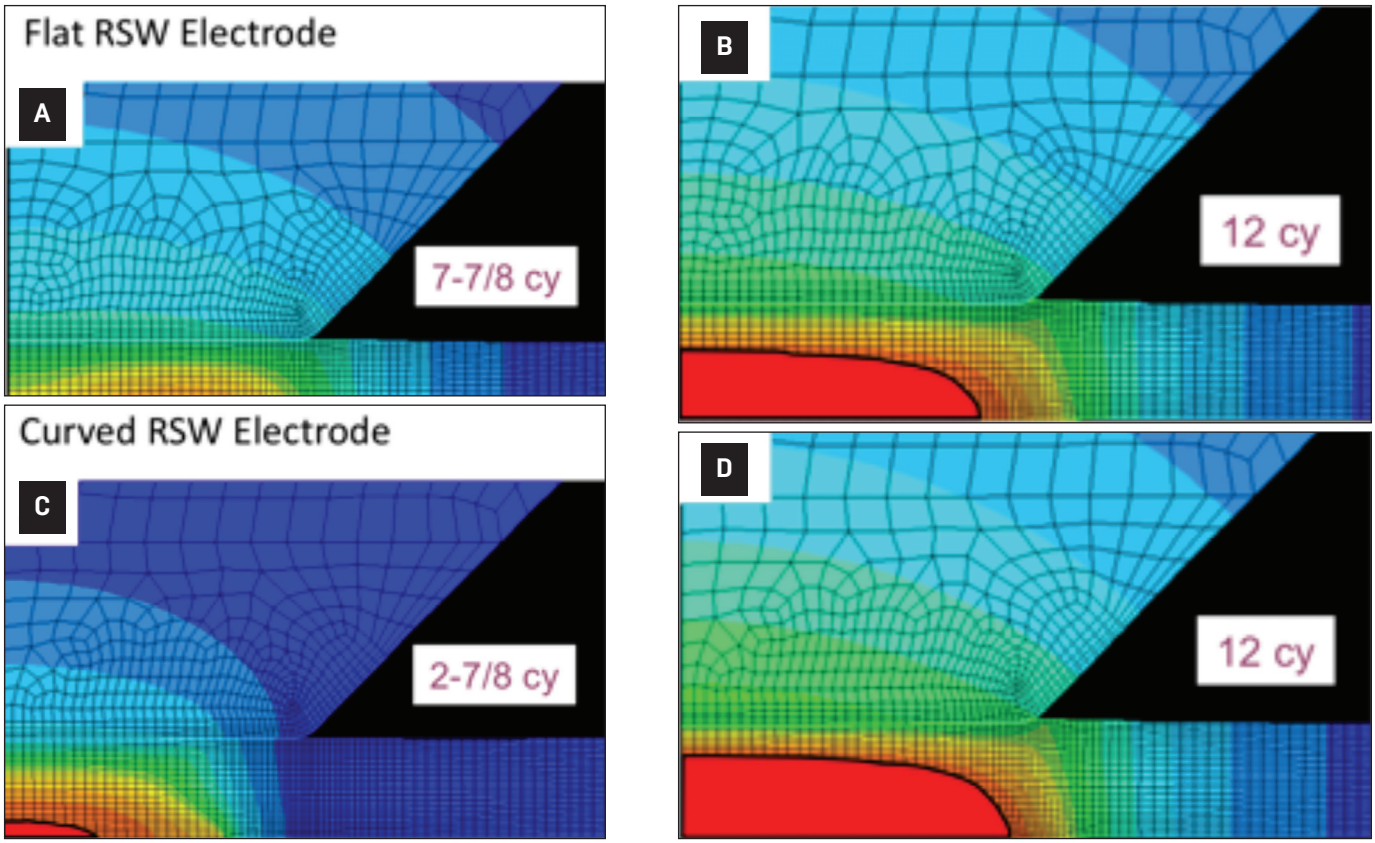

Fig. 2 — Predicted temperature distribution (blue — room temperature; red — melting point of steel) during spot welding of a steel sheet at a different number of current cycles is shown in a quarter symmetry. The results show that flat electrodes (A and B) lead to a toroidal-shaped weld pool after 7 ⅞ cycles, while the curved electrodes lead to stable hemispherical spot weld growth immediately after 2 ⅞ cycles for similar current levels.

try welded assembly and evolving residual stress and distortion. In another example, microstructural refinement in aluminum alloys was achieved by just changing the backing plate materials from stainless steel to copper (Ref. 32) for the same processing conditions. This approach had also been extended to stainless (Ref. 33) to modify the microstructure. In another example, microstructure and properties in steel welds were found to vary significantly on moving from stringer to weaving mode of welding, while keeping the same average heat input conditions (Ref. 34). This is attributed to the onset of local brittle zones due to transient variations in the thermal signature at localized regions. In another example, the role of initial microstructure (e.g., distribution of carbides and chemical segregation) in advanced high-strength steels (AHSS) and its response to welding was attributed to improved ballistic properties in comparison to welds made with homogeneous materials (Refs. 35, 36). Similarly, during spot welding a small change in the electrode curvature led to large changes in weld nugget development — Fig. 2. Using incrementally coupled electrical, thermal, and mechanical models, the above changes were attributed to the changes in the spatial and temporal variation of current density across the electrode and steel sheet interfaces. Although limited, the above examples clearly stress the need for in-situ monitoring of the geometry, material, and processing boundary conditions. With the advent of commercial data logging devices, rapid and mobile thermal, optical (Ref. 37), and phonon (Ref. 38) tools, it is indeed possible to define some aspects of the geometry, material, and boundary conditions.

Prediction of Heat and Mass Transfer

As early as the 1940s, it was clear that for qualification of welds, it is necessary to predict temperature distribution around arc welds. Rosenthal published a classic paper that solved the heat flow in a quasi-steady state condition in infinite or semiinfinite plates (Refs. 39, 40). The above solutions have been extended to other processes and conditions by various authors (Ref. 41). With the advent of computational hardware and finite element methodologies, the heat transfer models above were to consider specific geometries and boundary conditions, as well as transient conditions. For example, Yang and Babu (Ref. 27) used the finite element models to capture the transients (Fig. 3) in heat-transfer conditions during laser cladding of nickel-based alloys.

Although, the above models do not consider the fluid flow effects, they have been extensively used in industry The role of fluid flow on description of the melt pool shape was pioneered by researchers including Kou (Ref. 42), Zacharia (Ref. 43), and DebRoy (Ref.

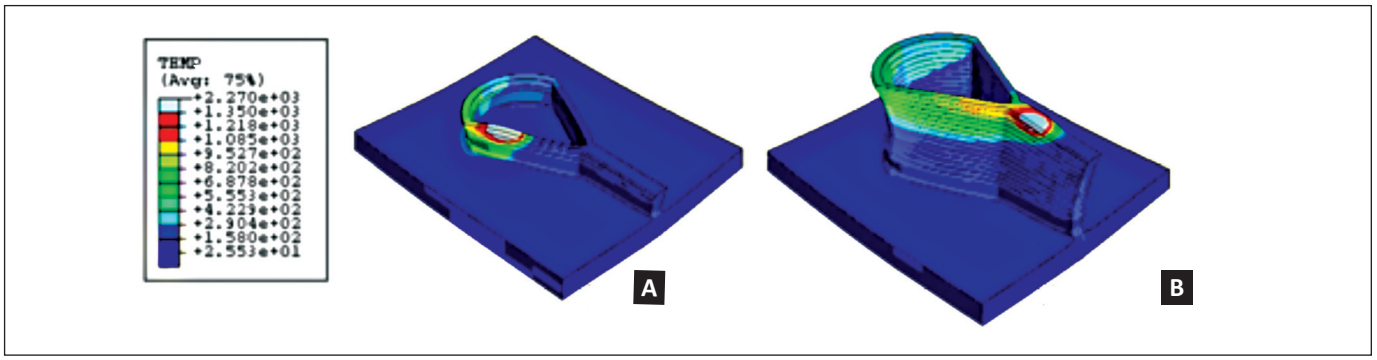

Fig. 3 — Predicted temperature distribution during laser cladding for repairing of nickel alloys at the following: A — Early stages; B — middle of the build. The calculations show the transients in temperature distribution due to changes in the heat sink brought about the change in the build geometry.

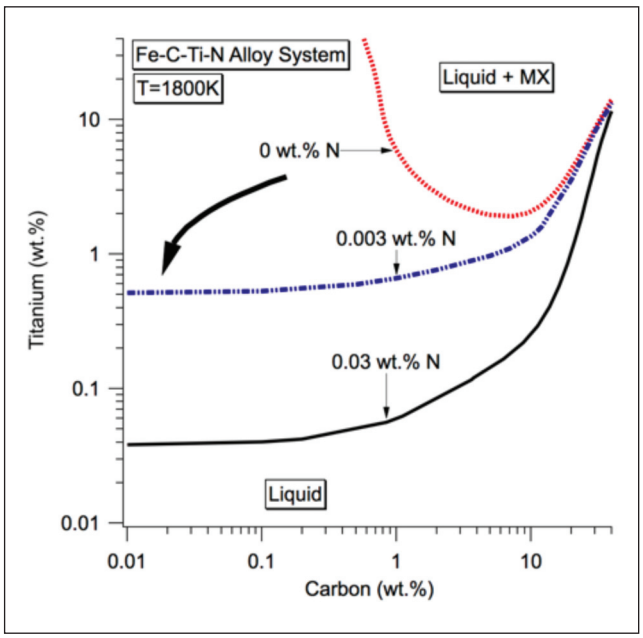

Fig. 4 — Calculated stability diagram for Ti(CN) carbo-nitride in steel melts as a function of titanium and carbon concentration with different levels of dissolved nitrogen showed the sensitivity to small additions of nitrogen to the system.

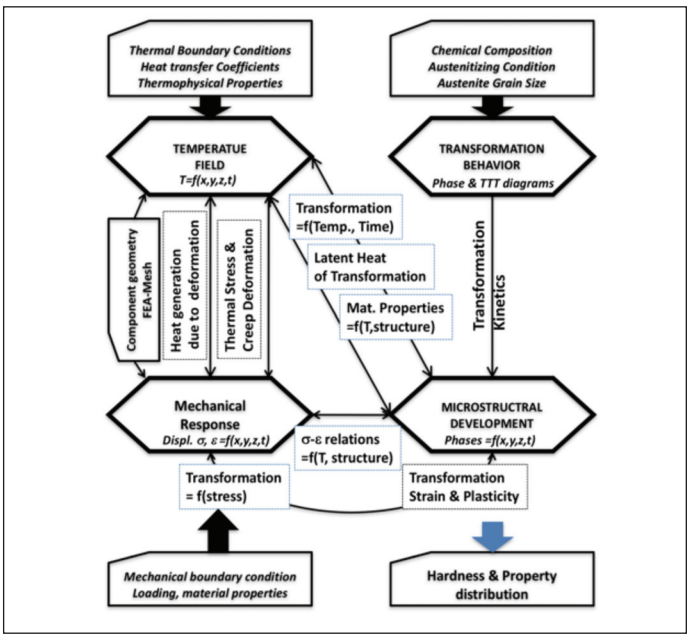

Fig. 5 — Schematic of integrated computational weld mechanics approach proposed by Kirkaldy (Ref. 72).

44). All of these models share a similar flow of information, starting with processing conditions (i.e., mode of energy delivery); material addition (e.g., welding wire feed rate); joint geometry; and defining the boundary conditions for conductive, convective, and radiative heat transfer. Then, for these boundary conditions, the melting, fluid flow, and cooling to ambient temperatures are calculated by solving the conservation of mass, momentum, and energy. The outputs of the model include temperature variations at different locations, melt pool shape, thermal gradients (G), and liquid-solid interface velocity (R). The above data can be used to predict the solidification, solid-state transformation, and deformation characteristics in the weld metal (WM) and heat-affected zones (HAZ).

Prediction of Phase Stability

The thermodynamic and kinetic framework for describing liquid-to-solid (Ref. 45) and solid-to-solid phase transformations (Ref. 46) are well established in physical metallurgy textbooks (Ref. 47). Based on many decades of research and development across the world, commercial solutions exist for calculating phase diagrams for multicomponent metals and ceramic systems. In the above theoretical construct, for calculating the phase diagrams and interface or interphase stabilities, the following equality (Equation 1) is assumed, i.e., the chemical potential of i^{th} element is the same at either side of the interface between the two phases, P1 and P2 (Refs. 48, 49).

$$\mu_i^{P1} = \mu_i^{P2} \qquad (1)$$

This equality is also known as the tie-line construction or common tangent between molar Gibbs energy vs. composition curves for two phases, in a graphical representation of the phase diagram. The chemical potential of the i^{th} element in a multicomponent system can be calculated using the follow-

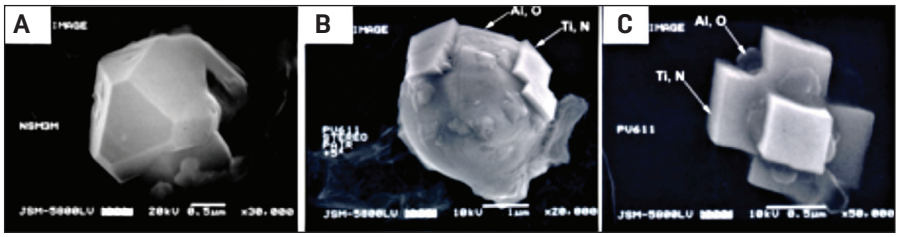

Fig. 6 — Scanning electron microscopy images from the following: A — High-Al weld exhibits AlN inclusion; B — low-Al weld shows both Al_2O_3 and Ti(CN) inclusions.

Table 1 — Composition of Self-Shielded Weld Metal (wt-%)

ID	C	Si	Mn	Si	Al	Ni	Ti	O	N	Balance
high-Al	0.234	0.28	0.50	0.28	1.70	0.02	0.003	0.006	0.064	Fe
low-Al	0.149	0.30	0.64	0.30	0.53	0.01	0.058	0.030	0.033	Fe

ing expression (Equation 2) that relates to the molar Gibbs free energy and partial derivative of the Gibbs free energy at a given temperature.

$$\mu_i^{P1} = G_{molar}^{P1} + \sum_{j=2}^{r}\left(\delta_{ij} - x_j\right)\frac{\partial G_{molar}^{P1}}{\partial xj};$$

where $\delta_{ij} = 0$ for i≠j and

$$\delta_{ij} = 1 \text{ for } i=j \qquad (2)$$

The molar Gibbs free energy of the phase P1 is given (Equation 3) by the contribution from the pure element (G_i^0), ideal mixing, and excess energy of mixing defined by the parameter Ω_{ij}^{v}.

$$G_{molar}^{P1} = \sum_i x_i G_i^0 + RT\sum_i x_i \log x_i + \sum_i \sum_{j>1} x_i x_j \sum_v \Omega_{ij}^{v}\left(x_i - x_j\right)^{v} \qquad (3)$$

In the above equation, R is the gas constant, T is the temperature, x_i corresponds to the mole fraction of i^{th} element in the solid solution, and v is a power factor that takes the value from zero to two. Similar equations also exist for the description of the molar free energy of compound. For example, it is possible to calculate the equilibrium between liquid steel and Ti(CN) carbonitride as a function of dissolved carbon, titanium, and nitrogen concentration — Fig. 4. These calculations may allow us to estimate the role of dissolved nitrogen on inducing a wide range of inclusions. Such diagrams can be used to develop an inoculation strategy to arrive at the equiaxed grain structures in welds (Ref. 50). With the above formulations, it is indeed possible to predict the multicomponent phase diagrams relevant to weld metal consumables, as a function of composition and temperature.

Prediction of Liquid-Solid Transformation

The solidification conditions during welding are related to the liquid-solid (l/s) interface instability. Phenomenological theories describing l/s interface stability under unidirectional thermal gradients are well known (Ref. 51) in the casting (Ref. 52) and welding literature (Ref. 24). It is indeed possible to predict columnar to equiaxed solidification transition (CET) as a function of thermal gradient ($G_{l/s}$) and *l/s* interface velocities ($V_{l/s}$)) based on dendrite tip temperature (T_d), with interface response function theories and by solving the coupled equations (Ref. 53) that describe the (k_v^i) kinetic solute partitioning coefficient, (m_v^i) nonequilibrium slope of the liquidus, dendrite tip radius (R), and ($c_{l/s}^i$) concentration at the *l/s* interface, as a function of $V_{l/s}$ and $G_{l/s}$.

$$k_v^i = \left(k_o^i + a_o\left[V_{l/s}/D_i\right]\right) / \left(1 + a_o\left[V_{l/s}/D_i\right]\right), \qquad (4)$$

$$m_v^i = m_o^i\left(1 - k_v^i\left[1 - ln\left\{k_v^i/k_o^i\right\}\right]\right) / \left(1 - k_o^i\right) \qquad (5)$$

$$4 + {}^2\Gamma\left(1/R^2\right) + \left(2\Sigma_i\, m_v^i Pe^i\left(1 - k_v^i\right)c_{l/s}^{i*}\xi_c^i\right) (1/R) + G_{s/i} = 0, \qquad (6)$$

where $\xi_c^i = 1 = 2k_v^i /$

$$\left(2k_v^i - 1 + \left(1 + \left(2\pi/Pe^i\right)\right)^{0.5}\right) \qquad (7)$$

$$c_{l/s}^{i*} = c_o^i\left(1 = \left[1 - k_v^i\right]Iv\left\{Pe^i\right\}\right) \qquad (8)$$

$$T_d = T_L + \Sigma_i\left(c_{l/s}^{i*}m_v^i - c_o^i m_o^i\right) = 2\Gamma/R - V_{l/s}/\mu - \left(G_{l/s}D_i/V_{l/s}\right) \qquad (9)$$

In Equations 4–9, k_o^i is the equilibrium partitioning coefficient between the liquid and solid, D_i is the interphase diffusivity, m_o^i is the equilibrium liquidus slope, a_o is the characteristic diffusion distance, Γ is the Gibbs-Thompson coefficient, Pe^i is the Peclet number given by $V_{l/s}/(2D_i)$, μ is the interface kinetic coefficient, and $Iv\{\}$ is the Ivantsov function that depends on the Peclet number. Using thermodynamic information for a multicomponent system, Equations 4–9 can be iteratively solved to predict the dendrite tip temperature and thereby constitutional supercooling, as well as CET in a wide range of alloy systems. These equations can be extended to nonequilibrium eutectic growth as well. This phenomenological model has been successfully applied to a wide range of multicomponent alloys (Ref. 54).

Fundamentals of these theories and extension to welding are reviewed in the paper by David and Vitek (Ref. 24). With the above formulations, one should be able to estimate the solidification morphologies (planar, columnar, equiaxed), dendrite arm spacing, texture, and alloying element segregation as a function of thermal gradients (G) and liquid-solid interface velocity (R), predicted by heat and mass transfer models.

Prediction of Solid-State Phase Transformation

The microstructural evolutions during welding of steels, titanium, and nickel alloys are also related to solid-

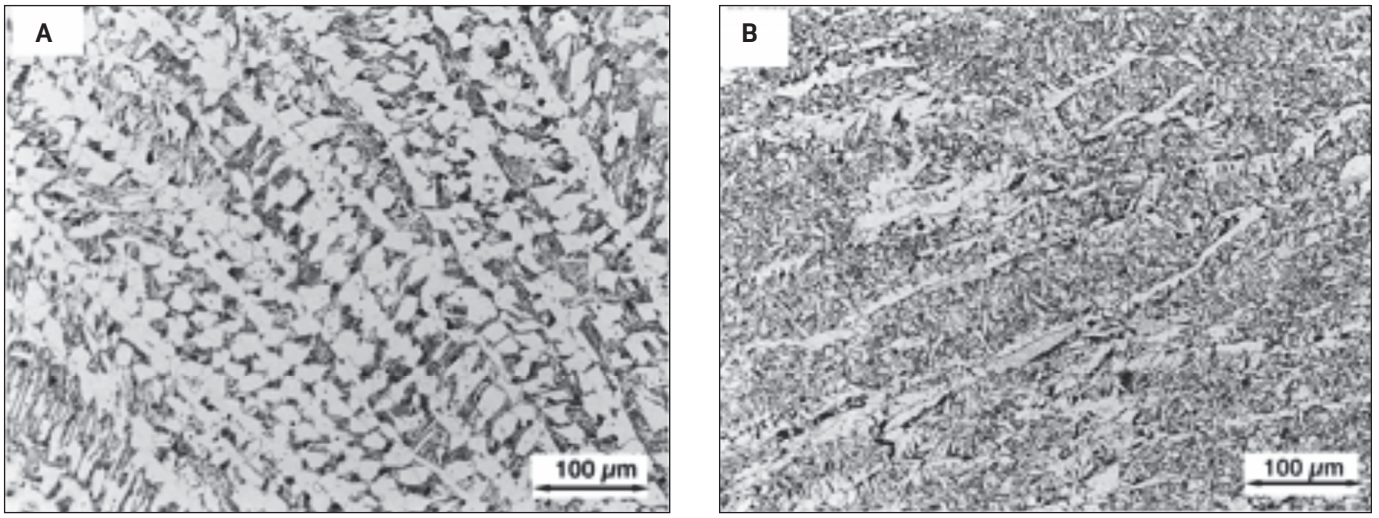

Fig. 7 — Optical microscopy images from A — High-Al weld shows skeletal columnar δ-ferrite interspersed with residual austenite that has transformed to bainitic microstructure. B — In contrast, the low-Al weld undergoes classic phase transformation to grain boundary ferrite and bainitic microstructure that is expected from 100% austenitic parent phase.

solid (s/s) interphase motion either through a reconstructive or displacive mechanism (Ref. 55). Let us revisit existing theories for interphase stabilities for s/s phase transformations originating from the classic papers of Hultgren published in 1947 (Ref. 56) and Coates (Refs. 57, 58). Under isothermal conditions, the velocity of the interface v_{int} between the two solid-state phases, P1 and P2, can be described by Equation 10.

$$\left(c_i^{P_1P_2} - c_i^{P_2P_1}\right)v_{int} = -D_i^{P_1}\left.\frac{dc_i}{dx}\right|_{int}^{P_1} - D_i^{P_2}\left.\frac{dc_i}{dx}\right|_{int}^{P_2} \quad (10)$$

In the above equation, c_i^{P1P2} is the interface concentration of solute "i" in the P_1 phase, and c_i^{P2P1} is the interface concentration of solute "i" in the P_2 phase. Similarly, D_i^{P1} and D_i^{P2} are the diffusivities of the solute in the P_1 and P_2 phases, respectively. In a multicomponent system, the above equations have to be solved simultaneously for all solute elements. Due to rapid cooling and/or large differences in the diffusivity, the equality represented by Equation 10 may break down and may induce constrained equilibrium. For example, paraequilibrium (Ref. 59) growth of ferrite into austenite in steel is controlled only by carbon diffusion, and the substitutional elements (Ref. 60) are configurationally frozen. In the case of displacive transformation, one can describe the same by coupling thermodynamics and theories of nucleation of martensite on lattice defects (Ref. 61). Bhadeshia et al. (Ref. 62) have extended to predict the microstructural evolution in low-carbon steel weld metals. In the early 1980s, due to limited access to thermodynamic data, a semi-empirical approach was based on carbon equivalence, austenite grain size, and the time taken to cool from 800° to 500°C (Refs. 63, 64). However, these phenomenological models are not capable of describing the 3D microstructural evolution. In this regard, the phase field models are very beneficial (Ref. 65) and have been used for describing both solidification and solid-state transformation in a unified way. With the above tools, it is possible to predict the microstructural features such as phase fractions, grain size, and morphology as a function of weld composition for a given thermal signature.

Prediction of Thermal Stresses and Plastic Deformation

One of the critical issues with welding is the evolution of residual stress distribution due to nonuniform accumulated plastic strains within the builds (Ref. 66). Under certain cases, thermal stresses can also lead to premature cracking during weld cooling conditions (Ref. 67). The plastic strain evolution during repeated thermal cycling is calculated based on thermal stresses brought about by macro-scale thermal gradients, local changes in thermal expansion coefficients, crystallographic misfit between phases, and constitutive stress-strain properties measured under isothermal conditions (Ref. 68). The constitutive properties for thermal simulation can be described either by experimental measurements or by calibrating constitutive relationships developed by Zener-Holloman (Ref. 69) or Johnson-Cook (Ref. 70) models. Recently, the Zener-Holloman model was used to describe the flow properties of Ti-6Al-4V alloys under torsional deformation conditions as a function of temperature and strain rate (Ref. 71). In addition, there are ongoing worldwide efforts to move away from the phenomenological models to describe the constitutive properties through crystal plasticity models (Ref. 72). With the above tools, it is indeed possible to predict the constitutive properties of metal deformation during typical thermomechanical conditions induced by spatial variation of thermal gradient and thermal signature typical to that of welding.

Integrated Process and Performance Models

Although each and every predictive tool is important in its own sense, for arriving at process-based quality, all of the above tools need to be integrated

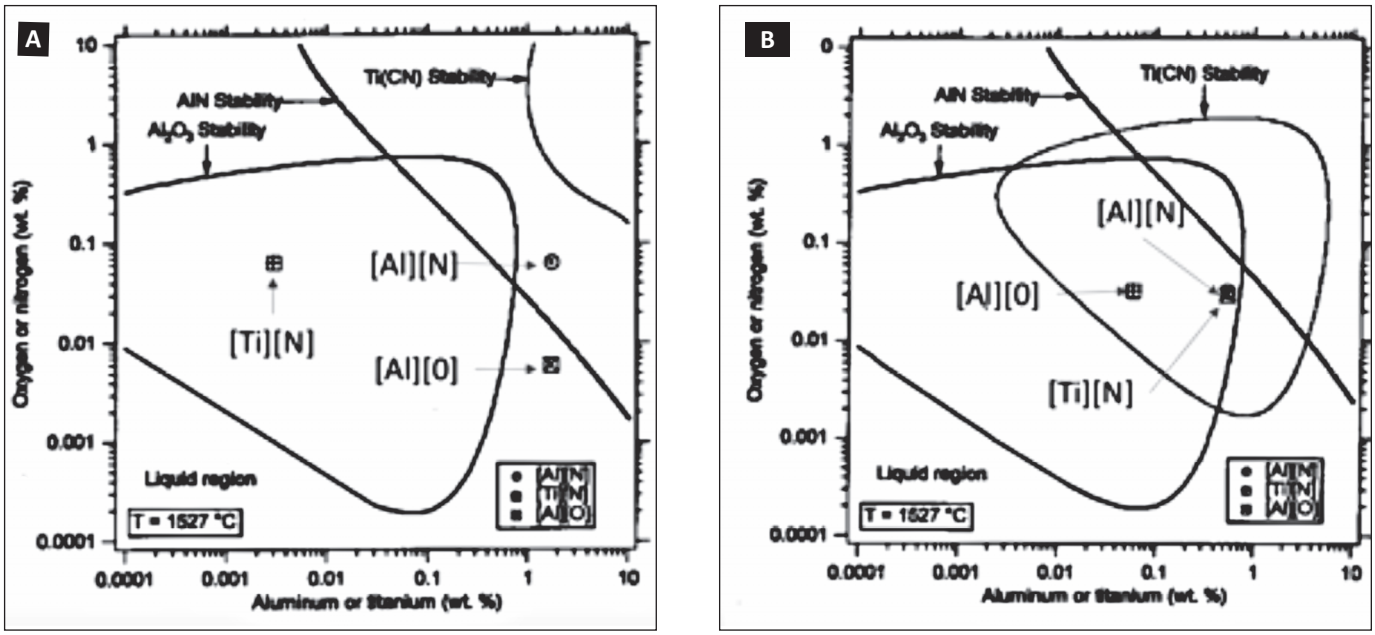

Fig. 8 — A — Calculated stability diagram for high-Al weld supports the preferential formation of AlN inclusions within liquid steel; B — similar calculations with low-Al weld composition shows the preferential formation of Al_2O_3 and Ti(CN) and not AlN.

within a single framework. This need was articulated by Kirkaldy in the 1990s (Ref. 73) with a classic diagram shown in Fig. 5 for predicting the steel weld properties. In his proposed integrated framework, hardness and property distributions, as well as residual stress and distortion in steel welds can be predicted as a function of boundary conditions (thermal, mechanical), thermo-physical-chemical properties by exchanging the information between submodels for heat and mass transfer, solidification, solid-state transformation, and mechanical response. As soon as one understands the spatial variations, the above data can also be mapped into a performance model to predict the static and dynamic properties of welded components (Ref. 74).

Interestingly, the above modeling framework has become the foundational tenet for many of the existing commercial solutions for integrated weld modeling. In 2007, the above integrated process modeling framework was deployed within a high performance computational framework capable of on-demand modeling over the internet (Refs. 75, 76). At this juncture, it needs to be stressed that applicability of these welding simulation tools always require some amount of calibration due to variability in thermo-physical-chemical properties (Ref. 77). In order to develop confidence in computational modeling, there is a need to develop verification and validation (V&V) standards. Recently, the above V&V document (Ref. 78) was developed and published by AWS, which enables the adoption of these tools by industries.

Furthermore, there is ongoing work on validation of residual stress prediction (Ref. 79) by the Nuclear Research Council (NRC) and Electric Power Research Institute (EPRI). These studies have shown the importance of material constitutive properties and the order of weld bead placement affecting the annealing on the variability of residual prediction. For example, the variations in predicted residual stresses may exceed more than ± 200 MPa (Ref. 80). In addition, extensive work is ongoing to understand the residual stress evolutions based on phase transformation kinetics and its effect on constitutive properties (Refs. 81, 82), especially for low-temperature-transformation (LTT) wires.

Unresolved Scientific Challenges

Based on the brief literature review on integrated process modeling, one may be tempted to conclude there are no scientific or technical challenges for process-based quality. However, there are two major challenges that need to be addressed with reference to microstructural evolution in welds, as described below.

Complex Alloying and Shielding Environments

In most of the published literature related to integrated process modeling, the compositions within the base metal or weld metal region are often considered to be uniform. Nevertheless, it is well known that small changes in the liquid-slag (Ref. 83) or liquid-gas (Ref. 84) reactions may lead to variations in deoxidizing elements (e.g., Ti and Al), which in turn may lead to large changes in inclusions, solidification, and solid-state transformation microstructure (Ref. 85), as well as associated properties (Refs. 86, 87).

In addition, by changing from nonreactive to reactive gas shielding, it is possible to induce in-situ alloying and arrive at hard particles to induce wear resistance (Ref. 88). Although there has been pioneering work by welding researchers to understand the liquid-slag reactions (Ref. 89), dissolution of gases (Refs. 90, 91), evaporation (Ref. 92), and condensation (Ref. 93), there are no integrated models to predict these reactions a-priori, without cali-

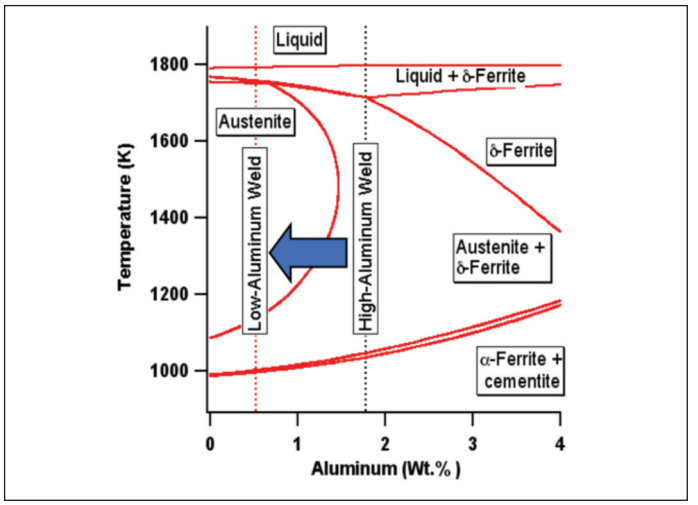

Fig. 9 — Calculated Fe-Al quasi-binary diagram shows a large change in the phase evolution as a function of temperature with small changes in dissolved aluminum concentrations.

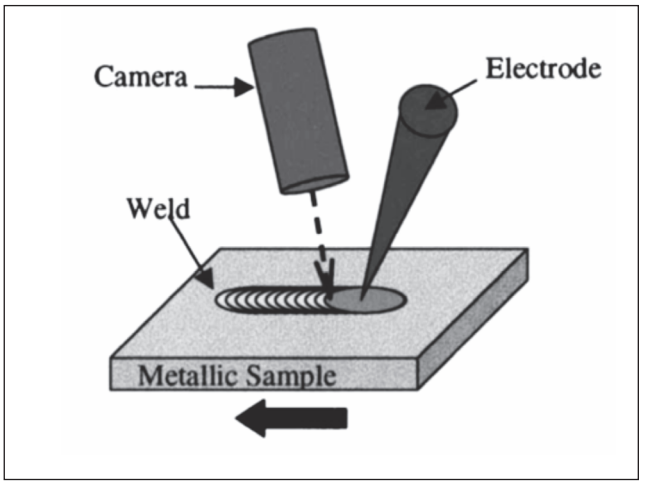

Fig. 10 — Schematic of the camera setup developed by Hall and Robino for the in-situ measurement of liquid-solid interface stability during welding (reproduced with permission from authors (Ref. 102)).

bration. Therefore, there is a need to improve the capability of computational thermodynamic tools to address the above phenomena.

Transients in Welding Conditions

In most of the engineering solutions relevant to welding, steady-state conditions are valid to predict thermomechanical changes. However, in certain cases involving manual welding for vertical and overhead configurations, automatic welding with weaving and varying geometrical cross sections, the above assumption may not be valid. These transients may lead to local changes in microstructures that may lead to scatter in properties (Ref. 94). Furthermore, during welding with large energy density, thermal gradients may exceed 10^6 K/m. Most of the phase stability and kinetic models for solid-state transformations were developed under isothermal conditions. Currently, the validity of the local equilibrium assumed by Equation 1 for these conditions is not known. Furthermore, in multipass welds, thermal signatures may induce repeated dissolution and growth under severe thermal gradients (Ref. 95). Therefore, there is a need to understand the effect of these transients and development of methodologies to track the same under in-situ conditions (Refs. 96, 97) and map the same to integrated process models to arrive at process-based quality.

Scientific Approaches to Address Challenges

In this paper, four case studies are presented with increasing complexities to demonstrate the approaches that can be used to address the fundamental challenges relevant to weld microstructural evolution. In order to provide continuity of the discussions, the first three case studies were restricted to self-shielded flux cored arc weld metal with an Fe-C-Al-Mn alloy system. The results from each case study in the Fe-C-Al-Mn alloy system build on the results from the previous ones. Finally, extension of these concepts to emerging metal additive manufacturing is also presented.

Case Study 1: Role of Thermodynamic and Kinetic Modeling

Problem Statement: Kotecki and Moll (Refs. 86, 87) found that inclusion formation and microstructural evolution in self-shielded flux cored arc (FCAW-S) welds were quite different from that of low-alloy steel welds made by submerged arc (SAW), shielded metal arc (SMAW), and gas metal arc (GMAW) welding. Since the FCAW-S processes do not use any form of gas shielding, the dissolved oxygen and nitrogen from atmosphere in the liquid steel is removed by large additions of aluminum. In this case study, the possibility of predicting these complex microstructural evolutions was explored using ThermoCalc® and DicTra® software (Refs. 98, 99).

Approach: Microstructural evolution in weld metal compositions with two different aluminum concentrations (Table 1) were characterized. Then the observed microstructural evolution was compared with the predictions from computational thermodynamic and kinetic models.

Results: Scanning electron microscopy showed welds with high aluminum concentration exhibited only AlN-type inclusions — Fig. 6A. In contrast, the weld with low aluminum concentration contained both Al_2O_3 and Ti(CN)-type inclusions — Fig. 6B, C. Interestingly, the high-Al welds also exhibited columnar δ-ferrite (BCC crystal structure) network interspersed with bainitic ferrite (α) microstructure that formed from stable austenite (γ) — Fig. 7A. This result suggests that high-Al welds do not go through 100% austenite phase field. In contrast, low-aluminum welds did not show any columnar ferrite network (Fig. 7B) and exhibited grain boundary ferrite and bainitic microstructure that forms directly from the 100% austenite phase field.

Physics-Based Modeling of Inclusion Formation: First, the ability to predict inclusion formations was analyzed with stability maps that depict the equilibrium between AlN, Al_2O_3 or Ti(CN), and liquid steel at 1527°C — Fig. 8A, B. The calculations were performed with ThermoCalc®

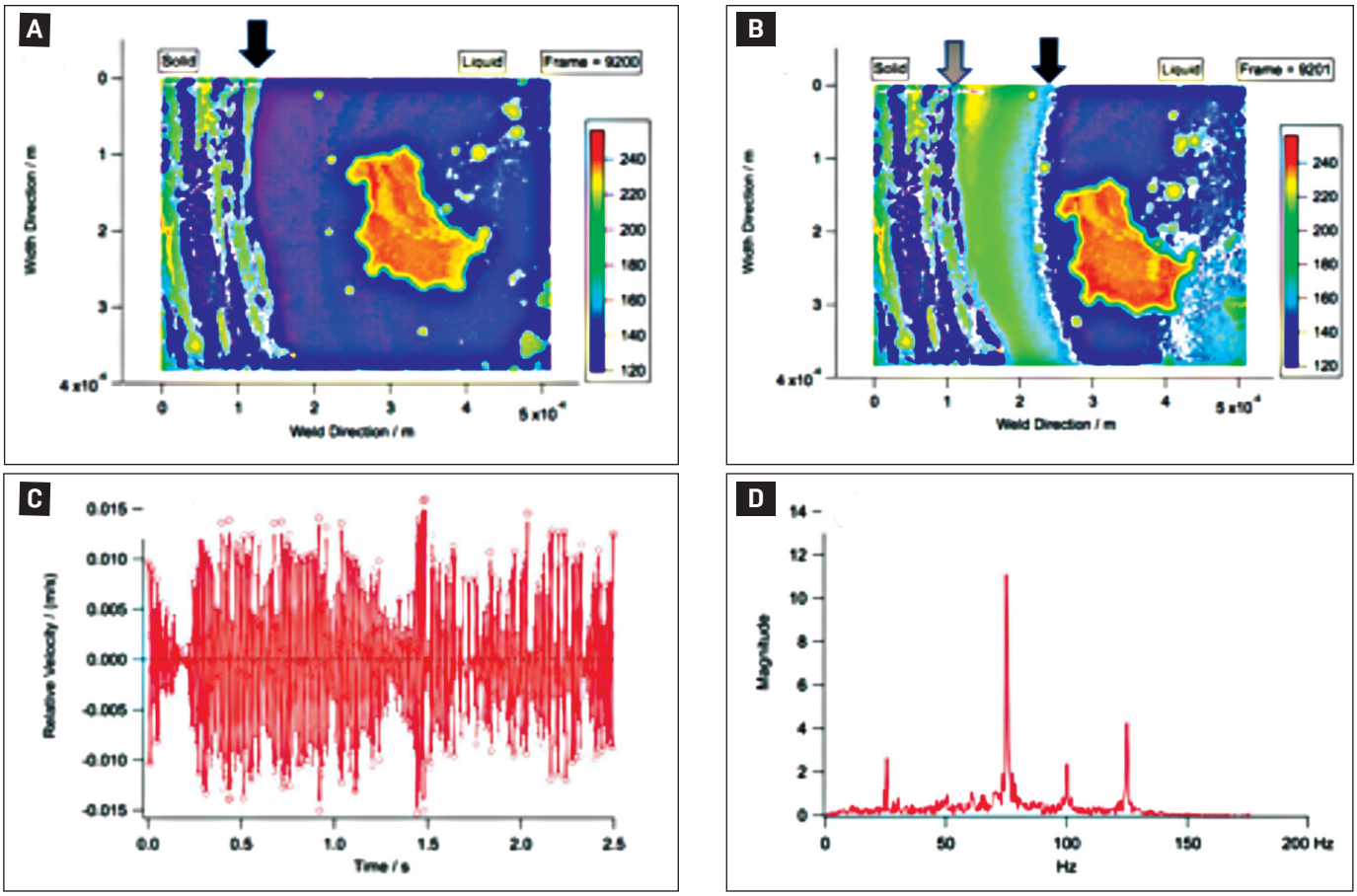

Fig. 11 — Overview of the liquid-solid interface instabilities during the pulsed GTAW process measured using in-situ optical method: A, B — Two successive frames showing the motion of large inclusions (orange color) and small inclusions (green color) within the liquid steel (blue regions). In addition, the same images show the motion of the band of the liquid-solid interface. C — Calculated temporal variation of the liquid-solid interface from the images show large scatter; D — the data shown in C is converted into frequency domain using DFFT analyses.

software that relies on foundational Equations 1 to 3. For the high-Al welds, the concentration of dissolved Al and N lies on the right side of the AlN stability line, which conforms to the tendency for the formation of AlN inclusions. In contrast, the concentrations of Al and O lie outside the stability loop for Al_2O_3. Similarly, the concentration of Ti and N fall outside the stability loop for the formation of Ti(CN) inclusions. The stability diagram also confirmed that with the reduction of aluminum concentration, the formation of Al_2O_3 and Ti(CN) is favored, while the formation of AlN is stifled in low-Al welds. It is indeed intriguing to notice that even with the presence of high aluminum concentrations, the Al_2O_3 formation is not possible. Careful analyses of thermodynamic description show that this effect is due to the 2nd order interactions (Ref. 100) between dissolved Al and O in the liquid steel, which stabilizes the liquid phase with reference to Al_2O_3.

Physics Based Modeling of Microstructural Evolution: Application of Fe-C phase diagram to high-Al welds would not have supported the retention of δ-ferrite at room temperature. However, the Fe-Al quasi-binary diagram (Fig. 9) calculated for the compositions shown in Table 1 shows interesting features. For high-Al welds, on cooling from high temperature, the liquid steel will transform first to δ-ferrite. With subsequent cooling to low temperature, the austenite will form at the liquid δ-ferrite dendrite boundaries. Subsequent cooling to low-temperature high-Al weld never enters the 100% austenite phase field. As a result, there is a high probability for the retention of δ-ferrite on cooling further. In contrast, the low-Al welds do enter into 100% austenite phase field and thereby promotes the formation of grain boundary and bainitic microstructure seen in other low-alloy steel welds. The above thermodynamic tendencies were also confirmed by calculating the growth of austenite into δ-ferrite as a function of weld cooling rate through kinetic models capable of describing the diffusion of C, Si, Mn, and Al between these two phases (Ref. 99).

Relevance to Process-Based Quality: The above examples show the ability of thermodynamic models to predict inclusion formation and microstructural evolution. At the same time, the results stress the need for a good thermodynamic description of liquid steel. For example, the thermodynamic data relevant to liquid steel, including the 2nd order interaction, was measured in the 1960s to 1970s by ladle metallurgy researchers (Ref. 101). Without this data, the models would have not been able to predict the absence of Al_2O_3 formation in high-Al welds. The

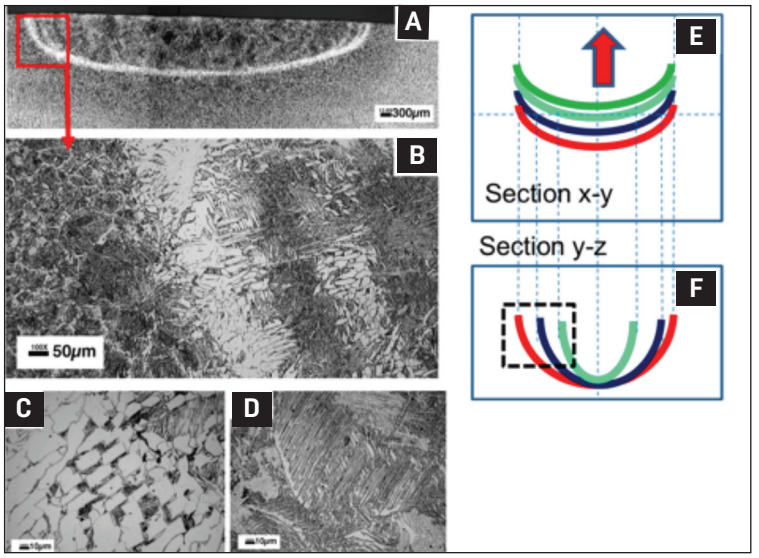

Fig. 12 — A — Cross section (Y-Z) of the pulsed GTA welds relevant to the data shown in Fig. 11. The images in B–D show the presence of an alternating band of δ-ferrite network and bainitic microstructure that forms from 100% austenite.

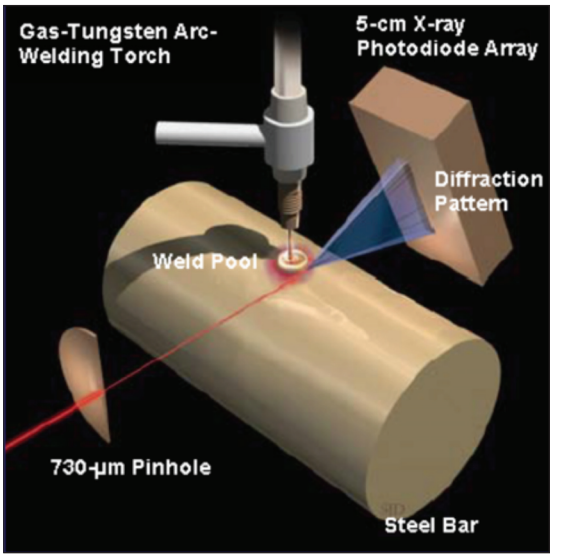

Fig. 13 — Schematic of the time-resolved X-ray diffraction experiments performed within a synchrotron beamline. The image was reproduced with permission from the authors of Ref. 97.

above example demonstrates the need for continued experimental measurements of thermodynamic properties of various phases in alloys relevant to welding and joining.

Case Study 2: Effect of Liquid-Solid Interface Transients

Problem Statement: The thermodynamic and kinetic models allowed us to predict the inclusion formation and microstructural evolution in welds made with normal steady-state conditions. However, the applicability of the model to transient conditions was not evaluated. For example, under pulsed welding conditions, one may experience local changes in thermal gradients and liquid-solid interface velocity. This case study focuses on the measurement of the transients in weld solidification conditions in an Fe-C-Al-Mn alloy system, specifically within high-Al welds.

Approach: In this research, autogenous gas tungsten arc (GTA) welds were made with the following conditions: 18.5 V, pulse peak current 130 A, pulse background current 90 A, pulse frequency of 300 Hz, welding speed 0.6 mm/s, and helium shielding. A high-speed in-situ monitoring system (Fig. 10) developed by Hall and Robino (Ref. 102) was used to track the instabilities of the liquid-solid interface. In this setup, the camera was mounted on a fixture attached to the weld arc and recorded at a time interval of 0.005 s. Therefore, the relative velocity between the camera and the weld pool was set at zero.

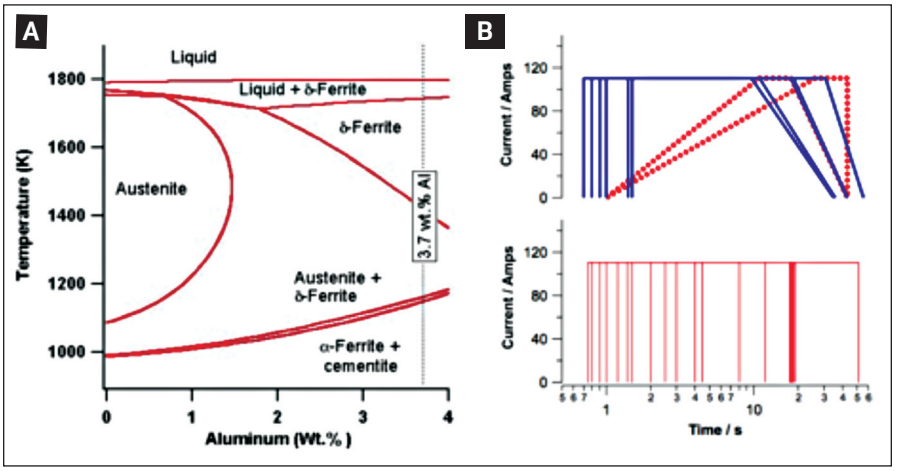

Fig. 14 — A — Fe-Al quasi-binary diagram shows the concentration of aluminum in the welds used for the in-situ TRXRD experiments; B — illustration of different spot welding experiments performed in conjunction with TRXRD experiments.

Results: The in-situ images were evaluated through standard image analysis tools (Ref. 103). Typical images from two sequential time frames are shown in Fig. 11A, B. Original black and white images were converted to color to illustrate various observed phenomena. First, the images show the motion of coarse and fine inclusions in the liquid region. Second, the snapshots also show alternating motion of the liquid-solid interface with reference to the camera location. The locations of these interface positions were extracted from a series of image frames. Since the relative velocity between camera and arc is zero, the motions of the interface are interpreted as growth and dissolution (Fig. 11C) reaching the rates of ±0.015 m/s. The above data were further analyzed using discrete fast Fourier transformation (FFT) algorithm. The analyses (Fig. 11D) show the pulsed interface motion occurs at different frequencies, i.e., 25, 75, 100, and 125 Hz. Currently, the reasons for such specific frequency evolutions are not understood.

The effect of such *l/s* oscillations on microstructural evolution was evaluated by optical microscopy — Fig. 12. The

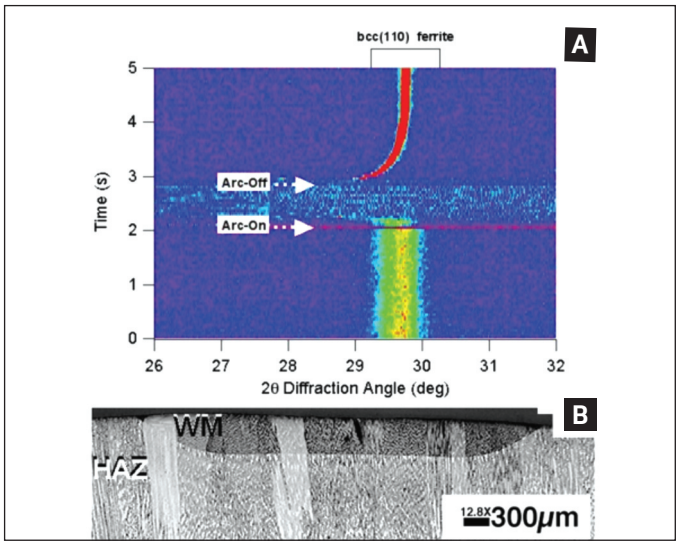

Fig. 15 — A — Image representation of the in-situ TRXRD data shows the presence of BCC peaks before and after the arc strike; B — optical micrograph confirms the presence of epitaxial columnar δ ferrite.

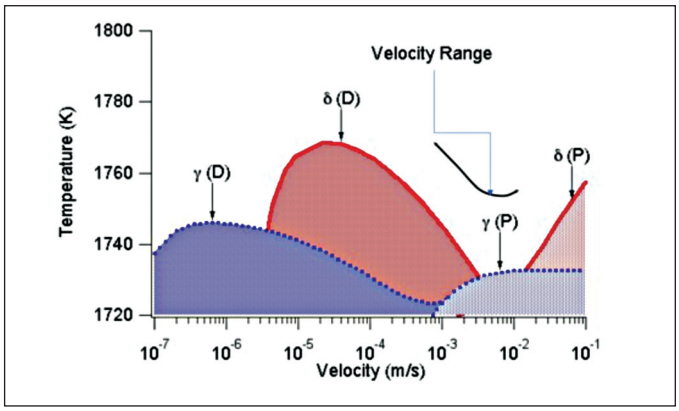

Fig. 17 — Comparison of calculated dendrite-tip and planar interface temperature for both δ-ferrite and γ-austenite using interface response function theories (Equations 4–9) and calibrated parameters given in reference shows scenarios that may lead to phase selection phenomenon in 3.7 wt-% Al self-shielded flux cored arc welds. The higher the interface or dendrite tip temperature, the higher the probability for formation of that phase with a given morphology.

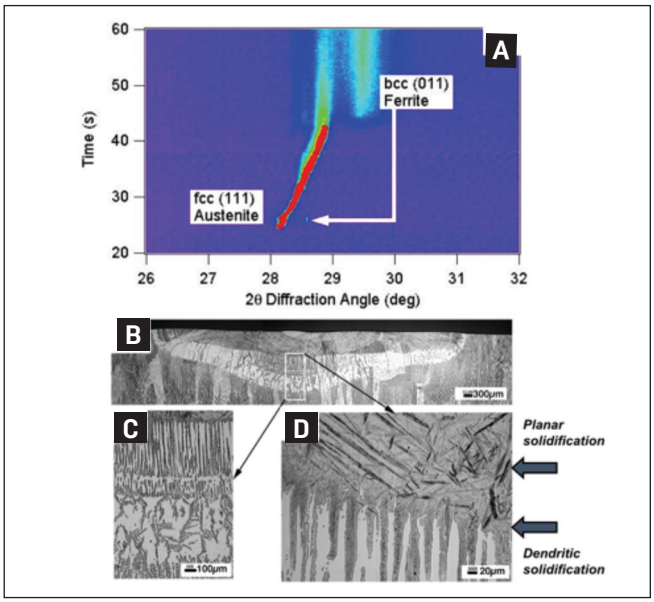

Fig. 16 — A — Image representation of the in-situ TRXRD data shows the lack of any diffraction peak before 20 s, confirming the presence of liquid before the arc-extinguishing event. After 20 s, when the arc extinguishes, a small speck of diffraction peak corresponding to δ-ferrite appears and disappears, while the austenite peak forms immediately and appears to be stable during cooling until 45 s. The cooling process is confirmed by the shift in the peak position. At about 45 s, the austenite diffraction is replaced by broad bcc peaks corresponding to martensite. B–D — Optical micrographs confirm the transition from columnar δ-ferrite to planar austenite, which transforms to martensite.

micrographs showed interesting phenomena of alternating arcs of columnar δ-ferrite and bainitic microstructure. This microstructure was interpreted as possible changes in the phase selection due to large changes in liquid-solid interface velocity (Ref. 104). At slow velocities, the equilibrium δ-ferrite is expected and with each and every acceleration of the interface nonequilibrium γ austenite might have manifested itself, similar to the classic work of Fukumoto and Kurz (Ref. 105).

Relevance to Process-Based Quality: The above data shows the solidification microstructural evolution is sensitive to the local thermal transients. Inability to describe the above transients in models may not allow us to predict the scatter in properties associated with the banded microstructure shown in Fig. 12. Therefore, it is important to track these changes using in-situ sensors and correlate to the scatter in microstructure and properties.

Case Study 3: In-Situ Analyses of Liquid-Solid Interface Instabilities

Problem Statement: Although we postulated that the changes in microstructure shown in Figs. 11 and 12 are due to local changes in liquid-solid interface velocity, there was no direct proof. To validate our hypothesis, in-situ time-resolved X-ray diffraction (TRXRD) experiments (Fig. 13) were performed using the setup developed by Elmer (Ref. 97). Initial experiments with high-Al welds confirmed that a large change in liquid-solid interface velocity will indeed induce transition from equilibrium δ-ferrite to nonequilibrium austenite (Ref. 106). At this juncture, the generality of the above phenomena for a wide range of alloy compositions was not understood and is the focus of the current case study.

Approach: To validate the above phenomena, a special Fe-C-Al-Mn alloy weld with higher aluminum concentration was selected for the TRXRD experiments. The new alloy composition is Fe-0.28C-0.45Mn-3.7Al (wt-%). The quasi-binary Fe-Al diagram (Fig. 14A) shows that in this alloy, the stability of δ-ferrite is greater than γ-austenite. Therefore, we expect that for a wide range of liquid-solid interface velocities, we should only see δ-ferrite solidification and phase selection to nonequilibrium γ-austenite should be highly improbable. The phase evolutions at the HAZ

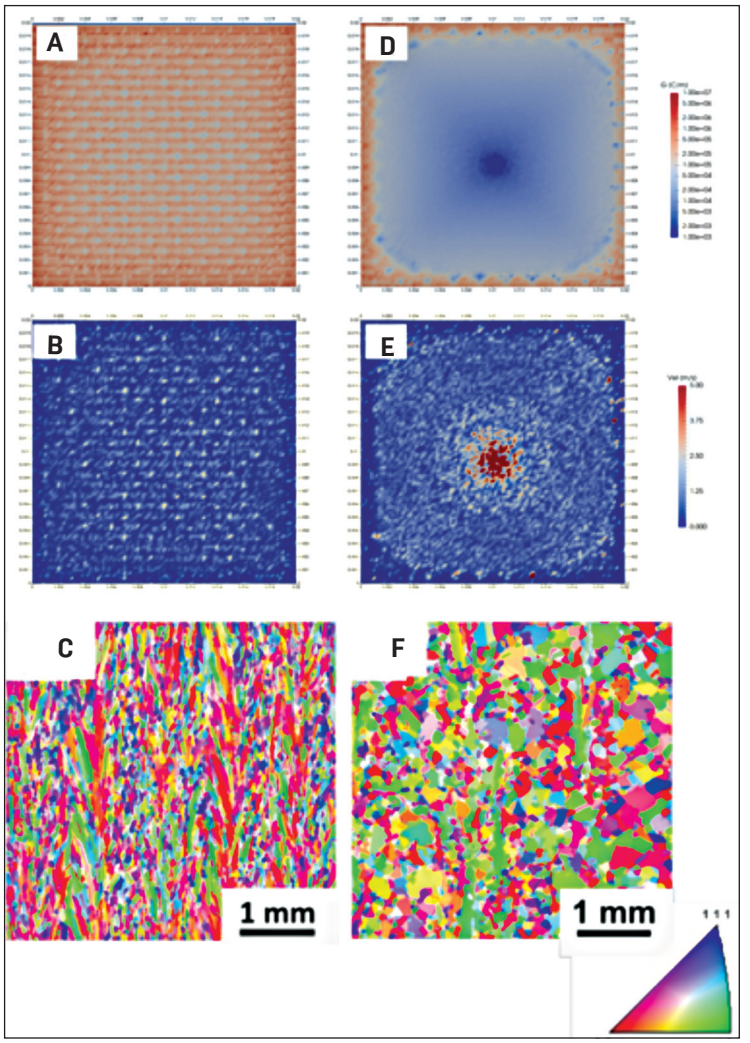

Fig. 18 — Calculated (A) G and (B) R for Cube 1, which uses a spot melt pattern leading to (C), the columnar grain region along the build direction. In contrast, (C) and (D) show the calculated G and R for Cube 2, which uses a spot melt pattern with shallow G and R, thereby inducing (E) an equiaxed microstructure (images were used with permission).

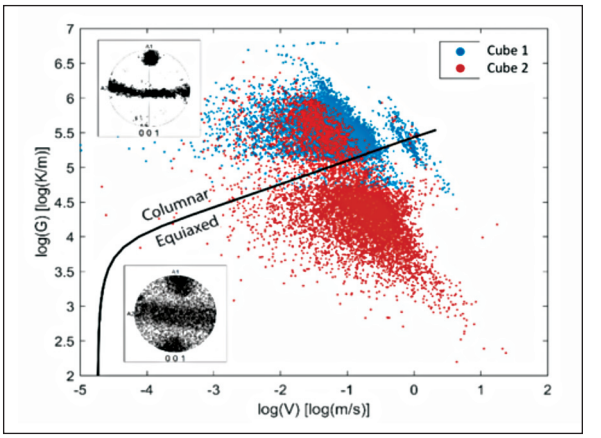

Fig. 19 — Overlay of calculated G and R for Cubes 1 and 2 on the columnar to equiaxed (CET) maps show that even with the scatter in the values, Cube 1 will predominantly lead to columnar microstructure and Cube 2 to equiaxed microstructure.

and WM were tracked for various spot welding experiments (Fig. 14B). The experiments considered 35 transient conditions relevant to spot welding including arc strike, arc ramp up, and arc ramp down (Ref. 106). In this paper, results from two conditions are discussed — Figs. 15, 16.

Results from Arc-Strike Experiment: In-situ diffraction data from arc-strike experiments are shown in Fig. 15A, B. Under this condition, the arc was switched on for 1 s and then extinguished. The diffraction data show the presence of BCC phase at room temperature. As soon as the arc strike was induced, the diffraction signals from the probed region were lost, indicating the formation of liquid. As soon as the arc was switched off, the diffraction peaks corresponding to (110) plane reemerged. The results confirmed that even under the nonequilibrium conditions that may induce large liquid-solid interface velocities, only δ-ferrite will form. Optical microscopy of the same spot weld shows epitaxial growth of ferrite from the HAZ — Fig. 15B. However, a quick analysis of the optical micrograph indicated that due to the small size of the weld metal region, the maximum velocity we could achieve would be in the order of only 3×10^{-4} m/s. As a result, one can postulate that higher liquid-solid interface velocities might not have been reached to induce nonequilibrium austenite phase selection.

Results from Current Ramp-Down Experiment: Previous research (Ref. 106) has shown that by forming a large weld pool and then using current ramp down, rapid liquid-solid interface velocity can be accessed. These conditions were imposed for new alloys. The diffraction data from the ramp-down conditions are shown in Fig. 16A. At the start of the ramp down of current, the data show no evidence for any crystal structure. However, at around 20 s, the data showed a brief formation of ferrite. At this time, the arc was extinguished, which leads to acceleration of the liquid-solid interface. Interestingly, the data show formation of nonequilibrium γ-austenite and transformation of the austenite to martensite on reaching low temperature at about 45 s. Similar experiments were performed on another build and the microstructural heterogeneity was evaluated — Fig. 16B–D.

The micrographs show the formation of equilibrium δ-ferrite close to the weld interface — Fig. 16B, C. However, with an increase in the liquid-solid interface velocity, instability in δ-ferrite dendrites was observed — Fig. 16D. Finally, most of the weld shows the formation of martensite laths that are larger than 100 μm, which could have only formed from large austenite grains. The above results suggest that we have accessed nonequilibrium γ-austenite with planar solidification. The above phase selection phenomena were analyzed using the interface response function theories outlined in the previous section (Ref. 104). The dendrite tip temperature for δ-ferrite and γ-austenite was calculated using calibrated parameters relevant to Equations 4–9. The results are shown in Fig. 17. The calculations show that for a given thermal gradient, it is possible to access the planar γ-austenite solidification, before

giving away to planar δ-ferrite.

Relevance to Process-Based Quality: Although the models have shown the feasibility of predicting these transient behaviors, the parameters used in Equations 4–9 have been calibrated. Therefore, extension of these models to other alloy systems must be accompanied by simple calibration experiments and heat transfer simulation with ramp-down and arc-strike experiments. Nevertheless, results from the above experiments showed it is indeed possible to control microstructure by spatially and temporally controlling thermal gradients and liquid-solid interface velocities.

Case Study 4: Extension to Powder Bed Additive Manufacturing

Problem Statement: It has been a dream of metallurgists to arrive at site-specific control of microstructures in near net shape components. The discussions in the previous section showed it is indeed possible to arrive at process-based quality by controlling microstructural heterogeneity. This microstructural control is possible in complex components if one can modify the spatial and temporal thermal signatures including thermal gradients and liquid-solid interface velocity. The emergence of powder bed additive manufacturing provides an opportunity to test out this hypothesis (Ref. 107).

Approach: Electron beam powder bed fusion (E-PBF) of Alloy 718 was selected for this case study. To induce different melt pool shapes, thermal gradients (G), and liquid-solid interface velocities (R), the beam spot-on time and location of the beam should be varied. A heat transfer model (Ref. 108) was used to design these spot melting strategies, a priori before the experiment. The predicted G and R are shown in Fig. 18. The first cube sample was designed (Fig. 18A, B) to induce columnar microstructure and the second cube sample was designed (Fig. 18D, E) to induce the equiaxed microstructure.

Results: These cube samples were produced by E-PBF melting of each layer with the spot melt patterns designed by models. The cube samples were then sectioned and analyzed using electron backscattered diffraction imaging. As expected, the first cube (Fig. 18C) showed a columnar microstructure and the second cube (Fig. 18F) showed an equiaxed microstructure. The above experiment was further verified by calculating the solidification maps using interface response function theories (Equations 4–9) and overlaying the calculated G and R values for Cubes 1 and 2 — Fig. 19. Even with a large amount of scatter, most of the G and R data from Cube 1 lay above the CET line confirming the tendency for the formation of columnar grains. Similarly, most of the data points from Cube 2 lay below the CET line cinforming the tendency for the formation of equiaxed grains. The above transitions have also been verified with in-situ infrared thermography and in complex geometries (Ref. 109).

Relevance to Process-Based Quality: The above example demonstrates that process-based quality is indeed achievable even under transient conditions, provided that we can reproduce these transients repeatedly by careful control of energy deposition and heat transfer. Recently, the above process-based quality framework, in conjunction with in-situ near-infrared imaging, was extended to qualification of topology optimized Ti6Al4V parts made by the E-PBF process (Ref. 110).

Future Directions

This review, results, and discussions demonstrate it is indeed possible to arrive at process-based quality of components much earlier than in 2040 as proposed in the AWS roadmap. Furthermore, the process-based quality framework must be extended to fusion welding, solid-state joining, brazing, soldering, and additive manufacturing by coupling integrated process models, in-situ process sensors, and the collection of all parameters relevant to process and other boundary conditions. The above data can be analyzed, tracked, and archived using emerging high-performance computing, cloud computing (Ref. 76), and data analytics (Ref. 111). Once we have developed and deployed proof-of-principle industrial standards based on process-based quality, the above approach can be extended to hybrid materials that join metals, polymers, ceramics, glass, and elastomers in different forms and functions (Ref. 112).

Summary and Conclusions

In this paper, the feasibility of process-based qualification of welded components was explored. A process-based qualification framework will involve concurrent activities ranging from modeling, making, and measuring with state-of-the-art computational and sensing tools. To succeed in this alternative approach to qualification, it is important to define all the boundary conditions including geometry, restraints, and the processing environment. Then, for given process conditions, an integrated modeling and sensing tool should be capable of predicting or describing the spatial and temporal variation of heat and mass transfer, solidification, solid-state transformation, and plastic deformation. With the above data, it is possible to predict the performance of welded components with minimal trial-and-error experimentation. Few examples were presented to bolster the argument for process-based quality of welded components. Two major scientific challenges were identified, i.e., variability in describing the alloying element concentration in weld metal and transients in thermal signatures, thermal gradient, and liquid-solid interface velocity. Approaches to address the above challenges are illustrated with four case studies.

In the first case study, the need for reliable multi-component thermodynamic data of liquid and solid phases are emphasized to describe inclusion formation and microstructural evolution in Fe-C-Al-Mn self-shielded flux cored arc welds. In the second case study, the role of in-situ monitoring by high-speed optical imaging to track the liquid-solid interface velocities and associated microstructural heterogeneity was presented. In the third case study, the role of in-situ time-resolved X-ray diffraction to probe the phase selection during transient welding was demonstrated. The data and analyses confirmed the importance ofspatial and temporal variations of the thermal gradient and liquid-solid interface velocity in forcing the equilibrium δ-ferrite or nonequilibrium γ-austenite solidification. Finally, with the above fundamental knowledge of weld solidification, site-specific control of microstructure was achieved in Alloy 718 builds made by electron beam powder bed fusion

technique. The results presented in this paper support the notion that process-based qualification of components made by welding and additive manufacturing is indeed achievable in the near future.

Acknowledgments

Research was sponsored by the U.S. Department of Energy, Office of Energy Efficiency and Renewable Energy, Advanced Manufacturing Office, under contract DE-AC05-00OR22725 with UT-Battelle LLC. This manuscript has been authored by UT-Battelle LLC under Contract No. DE-AC05-00OR22725 with the U.S. Department of Energy. The United States Government retains and the publisher, by accepting the article for publication, acknowledges that the United States Government retains a nonexclusive, paid-up, irrevocable, world-wide license to publish or reproduce the published form of this manuscript, or allow others to do so, for United States Government purposes. The Department of Energy will provide public access to these results of federally sponsored research in accordance with the DOE Public Access Plan (*http://energy.gov/downloads/doe-public-access-plan*). Author also thanks Dr. A. C. Hall (Sandia National Laboratories, Albuquerque, N.Mex.) and Dr. John Elmer (Lawrence Livermore National Laboratory, Livermore, Calif.) to use the data during the collaborative research. Author acknowledges the support of UT/ORNL Governor's Chair program of University of Tennessee, Knoxville.

References

1. Welding Technology Roadmap, Final Draft, September 2000, prepared by Energetics, The American Welding Society and Edison Welding Institute. The article can be accessed from the following internet location: *https://app.aws.org/research roadmap.pdf*

2. Babu, S. S. 2010. Introduction to integrated weld modeling. *ASM Handbook,* Vol. 22B, Metals Process Simulation, Eds. D. U. Furrer and S. L. Semiatin. ASM International.

3. Davis, J., Eagar, T., Porter, J., Bernaden, J., and Sarli, M. 2012. Smart manufacturing, manufacturing intelligence and demand-dynamic performance. *Computers and Chemical Engineering* 47: 145–156.

4. *Integrated Computational Materials Engineering: A Transformational Discipline for Improved Competitiveness and National Security.* 2008. The National Academies Press: Washington, DC.

5. Kalpakjian, S., and Schmid, S. 2013. *Manufacturing Engineering and Technology*, 7th Edition, Pergamon.

6. Saaksvuori, A., and Immonen, A. 2002. *Product Lifecycle Management*. Berlin, Germany: Springer-Verlag.

7. *Welding Handbook*, Vol. 1, Welding Technology. 1987. Miami, Fla.: American Welding Society.

8. *Metals Handbook*, Desk Edition, 2nd Edition. 1998. Materials Park, Ohio: ASM International.

9. AWS D1.1/D1.1M: 2015, *Structural Welding Code — Steel*. Miami, Fla.: American Welding Society.

10. AWS B2.1-1/8-010: 2015, *Standard for Welding Procedure Specification (SWPS)*. Miami, Fla.: American Welding Society.

11. Zhan, X., Ou, W., Wei, Y., and Jiang, J. 2016. The feasibility of intelligent welding procedure qualification system for Q345R SMAW. *Int. J. Adv. Manuf. Technol.* 83: 765–777.

12. AWS A5.5/A5.5M: 2014, *Specification for Low-Alloy Steel Electrodes for Shielded Metal Arc Welding*. Miami, Fla.: American Welding Society.

13. AWS C7.3:2016, AWS A5.5/A5.5M: 2014, *Process Specification for Electron Beam Welding*. Miami, Fla.: American Welding Society.

14. API Standard 1104, *Welding of pipelines and related facilities*, 21st edition, 2013. American Petroleum Institute

15. *Weld Quality: The Role of Computers*. 1988. Proceedings of an international conference on improvement of weldment control with reference to computer technology. Vienna, Austria: Pergamon Press.

16. Goldak, J. A., and Akhlaghi, M. 2005. *Computational Welding Mechanics*. Springer, USA.

17. Radaj, D. 1992. *Heat Effects of welding — Temperature Field, Residual Stress and Distortion*. Berlin, Germany: Springer-Verlag.

18. Wickle III, H. C., Zee, R. H., and Chin, B. A. 1999. A sensing system for weld process control. J. *Materials Processing Technology* 89-90: 254–259.

19. Chen, S. J., Huang, N., Liu, Y. K., and Zhang, Y. M. 2017. Machine assisted manual torch operation: System design, response modeling and speed control. *J. Intell. Manuf.* 28: 1249–1258.

20. Nilsiam, Y., Haselhuhn, A., Wijnen, B., Sanders, P., and Pearce, J. M. 2015. Integrated voltage-current monitoring and control of gas metal arc weld magnetic ball-jointed open source 3D printer. *Machines* 3: 339–351.

21. Goldak, J. A., Chakravarti, A., and Bibby, M. 1984. A new finite element model for welding heat sources. *Metall. Trans. B* 15: 299–305.

22. Kou, S., and Wang, Y. H., 1986. Computer simulation of convention in moving arc weld pools. *Metall. Trans. A* 17: 2271–2277.

23. DebRoy, T., and David, S. A., 1989. Physical processing in fusion welding. *Rev. Mod. Phys.* 67: 85–112.

24. David, S. A., and Vitek, J. M., 1989. Correlation between solidification parameters and weld microstructures. *Int. Mater. Reviews* 34: 213–245.

25. Ashby, M. F., and Easterling, K. E. 1982. A first report on diagrams for grain growth in welds. *Acta Metall.* 30: 1969–1978.

26. Bhadeshia, H. K. D. H., Svensson, L.–E., and Gretoft, B. 1985. A model for the development of microstructures in low-alloy steel (Fe-Mn-Si-C) weld deposits. *Acta Metall.* 33: 1271–1283.

27. Yang, Y., and Babu, S. S. 2010. An integrated model to simulate laser cladding manufacturing process for engine repair applications. *Welding in the World* 54: R298–R307.

28. Babu, S. S., Livingston, J., and Lippold, J. C. 2013. Physical simulation and microstructure evolution during friction stir processing of Ti6Al4V alloy. *Metallurgical and Materials Transactions A*, 44: 3577–3591.

29. Yang, Y., Babu, S. S., Vaze, S., Kikel, J. and Dewees, D. 2008. Cracking mitigation during buttering and cladding of a low alloy steel pipe. *Proceedings of Trends in Welding Research Conf.*, Pine Mountain, Ga. ASM International.

30. Withers, P. J., and Bhadeshia, H. K. D. H. 2001, Overview — Residual stress: Part 2 — Nature and origins. *Materials Science and Technology* 17: 366–375.

31. Pahkamma, A., Warmefjord, K., Karlsson, L., Soderberg, R., and Goldak, J. 2012. Combining variation simulation with welding simulation for prediction of deformation and variation of a final assembly. *J. Computing and Information Science and Engineering* 12; #021002.

32. Babu, S. S., Rajasekhar, M. V., and Achar, D. R. G. 1988. Studies on improving aluminum zinc magnesium alloy weld metal properties, presented at the international conference on Welding technology in Developing countries — Present status and future needs. Organized by University of Roorkee, India.

33. Rao, K. P. 1990. Effect of weld cooling rate on delta-ferrite content of austenitic weld metals. *Journal of Materials Science Letters* 90: 675–677.

34. Quintana, M. A., Babu, S. S., Major, J., and Dallam, C. 2010. Weld metal toughness — Sources of variation. *Proceedings of the 8th International Pipeline Conference*, IPC 2010, September 27–October 1, Calgary, Alberta, Canada.

35. Hanhold, B., Babu, S. S., and Cola, G. 2013. Investigation of heat affected zone softening in armor steels — Part 1: Phase transformation kinetics. *Science and Technology of Welding and Joining* 18: 247–252.

36. Hanhold, B., Babu, S. S., and Cola, G. 2013. Investigation of heat affected zone softening in armor steels — Part 2: Mechanical and microstructural heterogeneity. *Science and Technology of Welding and Joining* 18: 253–260.

37. Chen, J., Yu, X., Miller, R. G., and Feng, Z. 2015. In situ strain and temperature measurement and modeling during arc welding. *Sci. Technol. Weld. Join.* 20: 181–188.

38. Joseph A., Palanichamy, P., and Jayakumar, T. 2015. Evaluation of residual stresses in carbon steel weld joints by ultrasonic L_{cr} wave technique. *J. Nondestructive Evaluation* 34: #266.

39. Rosenthal, D. 1941. Mathematical theory of heat distribution during welding and cutting. *Welding Journal* 20(5): 220-s to 234-s.

40. Rosenthal, D. 1946. The theory of moving sources of heat and its application to metal treatments. *Trans. ASME* 68: 849–866.

41. Grong, O. 1997. *Metallurgical Modeling of Welding*, 2nd Edition. London, UK: Institute of Materials.

42. Tsai, M. C., and Kou, S. 1990. Electromagnetic-force-induced convection in weld pools with a free surface. *Welding Journal* 69(6): 241-s to 246-s.

43. Zacharia, T., David, S. A., Vitek, J. M., and DebRoy, T. 1989. Weld pool development during GTA and laser beam welding of Type 304 stainless steel, Part I — Theoretical analysis. *Welding Journal* 68(12): 499-s to 509-s.

44. Mundra, K., DebRoy, T., Babu, S. S., and David, S. A. 1997. Weld metal microstructure calculations from fundamentals of transport phenomena in the arc welding of low alloy steels. *Welding Journal* 76(4): 163-s to 171-s.

45. Kurz, W., and Fisher, D. J. 1998. *Fundamentals of Solidification*, 4th Edition, CRC Press.

46. Cahn, J. W. 1956. The kinetics of grain boundary nucleated reactions. *Acta Metallurgica* 4: 449–459.

47. Laughlin, D. E., and Hono, K. 2014. *Physical Metallurgy*, 5th Edition. Elsevier.

48. Saunders, N., and Miodownik, A. P. 1998. *Calculation of Phase Diagrams: A Comprehensive Guide*. Pergamon.

49. Hillert, M. 1998. *Phase Equilibria, Phase Diagrams and Phase Transformations —Their Thermodynamic Basis*. Cambridge University Press.

50. Villafuerte, J. C., Kerr, H. W., and David, S. A. 1995. Mechanisms of equiaxed grain formation in ferritic stainless steel gas tungsten arc welds. *Materials Science and Engineering A* 194: 187–191.

51. Trivedi, R., and Kurz, W. 1994. Dendrite growth. *International Materials Reviews* 39: 49–74.

52. Dantzig, J., and Rappaz, M. 2017. *Solidification*, 2nd Ed., EPFL Press.

53. Babu, S. S., Elmer, J. W., David, S. A., and Vitek, J. M. 2002. Time-resolved X-ray diffraction investigation of primary weld solidification in Fe-C-Al-Mn steel welds. *Acta Materialia* 50: 4763–4781.

54. Fukumoto, S., and Kurz, W. 1999. Solidification phase and microstructure selection maps for Fe-Cr-Ni alloys. *ISIJ International* 39: 1270-1279.

55. Babu, S. S. 2009. Thermodynamic and kinetics models for describing microstructure evolution during joining of advanced materials. *International Materials Reviews* 54: 333–367.

56. Hultgren, R. 1947. Isothermal transformation of austenite. *Trans. AIME* 39: 915–1005.

57. Coates, D. E. 1972. Diffusion-controlled precipitate growth in Ternary-systems — 1. *Metallurgical Transactions* 3: 1203–1212.

58. Coates, D. E. 1972. Diffusion-controlled precipitate growth in Ternary-systems — 2. *Metallurgical Transactions* 4: 1077–1086.

59. Babu, S. S., Hono, K., and Sakurai, T. 1994. APFIM study of the partitioning of substitutional elements during tempering of a low alloy steel martensite. *Metall. Trans. A.* 25A: 499–508.

60. Aaronson, H. I., Domain, H. A., and Pound, G. M. 1966. Thermodynamics of austenite — Proeutectoid ferrite transformation — 2: Fe-C-X alloys. *Trans. of the Met. Soc. of AIME*, Vol. 236, p. 768.

61. Ghosh, G., and Olson, G. B. 2001. Computational thermodynamics and kinetics of martensitic transformations. *Journal of Phase Equilibria* 22: 199–207.

62. Bhadeshia, H. K. D. H., Svensson, L. E., and Gretoft, B. 1985. The influence of alloying elements on the formation of allotriomorphic ferrite in low-alloy steel weld deposits. J. *Materials Science Letters* 4: 305–308.

63. Ion, J. C., Easterling, K. E., and Ashby, M. F. 1984. A 2nd report on diagrams of microstructure and hardness for heat-affected-zone in welds. *Acta Metallurgica* 32: 1949–1962.

64. Loberg, B., Nordgren, A., Strid, J., and Easterling, K. E. 1984, The role of alloy composition on the stability of nitrides in Ti-microalloyed steels during weld thermal cycles. *Metall. Trans. A.* 15A: 33–41.

65. Ohno, M., Yamaguchi, T., Sato, D., and Matsuura, K. 2013. Existence or nonexistence of thermal pinning effect in grain growth under temperature gradient. *Computational Materials Science* 69: 7–13.

66. Feng, Z., Wang, X. L., David, S. A., and Sklad, P. S. 2007. Modeling of residual stresses and property distributions in friction stir welds of aluminum alloy 6061-T6. *Sci. Technol. Weld. Joining* 12: 348–356.

67. Feng, Z., David, S. A., Zacharia, T., and Tsai, C. L. 1997. Quantification of thermomechanical conditions for weld solidification cracking. *Sci. Technol. Weld. Joining* 2: 11–19.

68. Heinze, C., Pittner, A., Rethmeier, M., and Babu, S. S. 2013. Dependency of martensite start temperature on prior austenite grain size and its influence on welding-induced residual stresses. *Computational Materials Science* 69: 251–260.

69. Schmidt, H., and Hattel, J. 2005. A local model for the thermomechanical conditions in friction stir welding. *Modelling Simul. Mater. Sci. Eng.* 13: 77–93.

70. Johnson, G. R., and Cook, W. H. 1985. Fracture characteristics of three metals subjected to various strains, strain rates, temperatures and pressures. *Engineering Fracture Mechanics* 21: 31–48.

71. Semiatin, S. L., and Bieler, T. R. 2001. The effect of alpha platelet thickness on plastic flow during hot working of Ti-6Al-4V with a transformed microstructure. *Acta Mater.* 49: 3565–3573.

72. Roters, F., Eisenlohr, P., Kords, C., Tjahjanto, D. D., Diehl, M., and Raabe, D. 2012. DAMASK: the Düsseldorf advanced Material Simulation Kit for studying crystal plasticity using an FE baser or a spectral numerical solver. *Procedia IUTAM* 3: 3–10.

73. Kirkaldy, J. S. 1991. Diffusion-controlled phase transformations in steels — Theory and applications. *Scand. J. Metall.* 20: 50–61.

74. Yang, Y. P., Babu, S. S., Orth, F., and Peterson, W. 2008. An integrated computational model to predict the mechanical behavior of spot welds. *Science and Technology of Welding and Joining* 13: 232–239.

75. Yang, Y., Zhang, W., Gan, W., Khurana, S. P., Xu, J. and Babu, S. S. 2008. Online software tool for predicting weld residual stress and distortion. *ASME 2008 Pressure Vessels and piping Conference*, Vol. 6, Materials and Fabrication, Parts A and B, PVP2008-61123, pp. 279–288.

76. Babu, S. S., Conrardy, C., Khurana, S. P., Zhang, W., and Gan, W. 2012. Remote high performance computing materials joining and material forming modeling system and method. U.S. Patent, #8,301,286 B2.

77. Pittner, A., Weib, D., Schwenk, C., and Rethmeier, M. 2008. Methodology to improve applicability of welding simulation. *Science and Technology of Welding and Joining* 13: 496–508.

78. AWS A9.5:2013, *Guide for Verification and Validation in Computation Weld Mechanics*. Miami, Fla.: American Welding Society.

79. Fredette, L. F., Broussard, J. E., Kerr, M., and Rathbun, H. J. 2011.

NRC/EPRI Welding Residual Stress Validation Program — Phase III details and findings. *Proceedings of PVP2011, 2011 ASME Pressure Vessels and Piping Division Conference*, July 17–21, Baltimore, Md.

80. Rathbun, H. J., Fredette, L. F., and Rudland, D. L. 2011. NRC welding residual stress validation program international round robin program and findings. *Proceedings of PVP2011, 2011 ASME Pressure Vessels and piping Division Conference*, July 17-21, Baltimore, Md.

81. Caron, J., Heinz, C., Schwenk, C., Rethmeier, M., Babu, S. S., and J. C. Lippold. 2010. Effect of continuous cooling transformation variations on numerical calculation of welding induced residual stresses. *Welding Journal* 89(7): 151-s to 160-s.

82. Heinze, C., Pittner, A., Rethmeier, M., and Babu, S. S. 2013. Dependency of martensite start temperature on prior austenite grain size and its influence on welding-induced residual stresses. *Computational Materials Science* 69: 251–260.

83. Babu, S. S., David, S. A., Vitek, J. M., Mundra, K., and DebRoy, T. 1995. Development of macro- and microstructures of C–Mn low alloy steel welds — Inclusion formation. *Materials Science and Technology* 11: 186–199.

84. Babu, S. S., Reidenbach, F., David, S. A., Böllinghaus, Th., and Hoffmeister, H. 1999. Effect of high-energy-density welding processes on inclusion and microstructure formation in steel welds. *Science and Technology of Welding and Joining* 4: 63–73.

85. Song, H. Y., Evans, G. M., and Babu, S. S. 2014. Effect of microstructural heterogeneities on scatter of toughness in multi-pass weld metal of C-Mn steels. *Science and Technology of Welding and Joining* 19: 376–384.

86. Kotecki, D. J., and Moll, R. A. 1970, A toughness study of steel weld metal from self shielded flux-cored electrodes — Part 1. *Welding Journal* 49(4): 157-s to 165-s.

87. Kotecki, D. J., and Moll, R. A. 1972. A toughness study of steel weld metal from self shielded flux-cored electrodes — Part II. *Welding Journal* 51(3): 138-s to 155-s.

88. Babu, S. S., Kelly, S. M., Murugananth, M., and Martukanitz, R. P. 2006. Reactive gas shielding during laser surface alloying for production of hard coatings. *Surface Coating and Technology* 200: 2663–2671.

89. Brandi, S., Taniguchi, C., and Liu, S. 1991. Analysis of metal transfer in shielded metal arc welding. *Welding Journal* 70(10): 261-s to 270-s.

90. Palmer, T. A., and DebRoy, T. 2000. Numerical modeling of enhanced nitrogen dissolution during gas tungsten arc welding. *Metallurgical and Materials Transactions B* 31: 1371–1385.

91. Elmer J. W., Vaja, V., Carlton, H. D., and Pong, R. 2015. The effect of Ar and N_2 shielding gas on laser weld porosity in steel stainless steel and nickel. *Welding Journal* 94(10): 313-s to 325-s.

92. He, X., Norris, J. T., Fuerschbach, P. W., and DebRoy, T. 2006. Liquid metal expulsion during laser spot welding of 304 stainless steel. J. *Phys. D: Appl. Phys.* 39: 525–534.

93. Khan, P. A. A., and DebRoy, T. 1984. Alloying element vaporization and weld pool temperature during laser welding of AISI 202 stainless steels. *Metall. Trans. B* 15B: 641–644.

94. Quintana, M. A., Babu, S. S., Major, J., and Dallam, C. 2010. Weld metal toughness — Sources of variation. *Proceedings of the 8th International Pipeline Conference, IPC 2010*, Sept. 27–Oct. 1. Calgary, Albera, Canada.

95. Hong, T., DebRoy, T., Babu, S. S., and David, S. A. 2000. Modeling of inclusion growth and dissolution in the weld pool. *Metallurgical Transactions B* 31: 161–169.

96. Smith, R. J., Li, W., Coulson, J., Clark, M., Somekh, M. G., and Sharples, S. D. 2014. Spatially resolved acoustic spectroscopy for rapid imaging of material microstructure and grain orientation. *Measurement Science and Technology* Vol. 25, #055902.

97. Elmer, J. W. 2008. A new path forward for understanding microstructural evolution during welding. *Welding Journal* 87(6): 149-s to 168-s.

98. Quintana, M. A., McLane, J., Babu, S. S., and David, S. A. 2001. Inclusion formation in self shielded flux-cored arc welds. *Welding Journal* 80(4): 98-s to 105-s.

99. Babu, S. S., David, S. A., and Quintana, M. A. 2001, Modeling microstructure evolution in self-shielded flux cored arc welds. *Welding Journal* 80(4): 91-s to 97-s.

100. Babu, S. S., David, S. A., Vitek, J. M., Mundra, K., and DebRoy, T. 1999. A model for inclusion formation in low alloy steel welds. *Science and Technology of Welding and Joining* 4: 276-284.

101. *The Making, Shaping and Treating of Steel*, 10th Edition, United States Steel. 1985. Published by the Association of Iron and Steel Engineers.

102. Hall, A. C., and Robino, C. V. 2004. Association of microstructural features and rippling phenomenon in 304 stainless steel gas tungsten arc welds. *Science and Technology of Welding and Joining* 9: 103–108.

103. Babu, S. S., Specht, E. D., David, S. A., Karapetrova, J., Zschak, P., Peet, M., and Bhadeshia, H. K. D. H. 2005. In-situ observations of lattice parameter fluctuations in austenite and transformation to bainite. *Metal. Mater. Trans. A* 36A: 3281–3289.

104. Babu, S. S., Elmer, J. W., David, S. A., and Quintana, M. 2002. In-situ observations of nonequilibrium austenite formation during weld solidification of Fe-C-Al-Mn low alloy steel. *Journal of Proceedings of Royal Society (Mathematical and Physical Sciences) A* 458: 811–821.

105. Fukumoto S., and Kurz, W. 1999. Solidification phase and microstructure selection maps for Fe-Cr-Ni alloys. *ISIJ International* 39: 1270–1279.

106. Babu, S. S., Elmer, J. W., Vitek, J. M., and David, S. A. 2002. Time-resolved X-ray diffraction investigation of primary weld solidification in Fe-C-Al-Mn steel welds. *Acta Materialia* 50: 4763–4781.

107. Sames, W., List, F. A., Pannala, S., Dehoff, R. R., and Babu, S. S. 2016. The metallurgy and processing science of metal additive manufacturing. *International Materials Reviews* 61: 315–360.

108. Plotkowski, A., Kirka, M. M., and Babu, S. S. 2017. Verification and validation of a rapid heat transfer calculation methodology for transient melt pool solidification conditions in powder bed metal additive manufacturing. *Additive Manufacturing* 18: 256–268.

109. Raplee, J., Plotkowski, A., Kirka, M. M., Dinwiddie, R., Okello, A., Dehoff, R. R., and Babu, S. S. 2017. Thermographic microstructure monitoring in electron beam additive manufacturing. *Sci. Rep.* 7: #43554.

110. Yoder, S., Morgan, S., Barnes, E., Kinzy, C., Nandwana, P., Kirka, M. M., Babu, S. S., Paquit, V., and Dehoff, R. R. 2017. Qualification of topology optimized Ti-6Al-4V components made by electron beam powder melting process. Submitted for publication in *Additive Manufacturing*.

111. Powers, S. A., Dehoff, R. R., Paquit, V. C., Steed, C. A., and Kistler, D. E. 2016. Application of data analytics to additive manufacturing. *Conference: 11th INFORMS Workshop on Data Mining and Decision Analytics (DM-DA 2016)*. Nashville, Tenn.

112. Ashby, M. F. 2005. Hybrids to fill holes in material property space. *Philosophical Magazine* 85: 3235–3257.

SUDARSANAM SURESH BABU is with Department of Mechanical, Aerospace and Biomedical Engineering, Tickle College of Engineering, The University of Tennessee, Knoxville, Tenn. He is also with Manufacturing Demonstration Facility, Energy and Transportation Sciences Division, Oak Ridge National Laboratory, Oak Ridge, Tenn.

Paper based on 2017 Comfort A. Adams Lecture, which was delivered on November 6, 2017, at the AWS Annual Convention, during FABTECH in Chicago, Ill.